How to cite: *Angew. Chem. Int. Ed.* **2024**, *63*, e202410998
doi.org/10.1002/anie.202410998

Contrast Agents | Hot Paper

Small, Fluorinated Mn^{2+} Chelate as an Efficient ^{1}H and ^{19}F MRI Probe

Zoltán Garda, Frédéric Szeremeta, Océane Quin, Enikő Molnár, Balázs Váradi, Rudy Clémençon, Sandra Même, Chantal Pichon, Gyula Tircsó, and Éva Tóth**

Abstract: We explore the potential of fluorine-containing small Mn^{2+} chelates as alternatives to perfluorinated nanoparticles, widely used as ^{19}F MRI probes. In **MnL1**, the cyclohexanediamine skeleton and two piperidine rings, involving each a metal-coordinating amide group and an appended CF_3 moiety, provide high rigidity to the complex. This allows for good control of the Mn–F distance ($r_{MnF} = 8.2 \pm 0.2$ Å determined from ^{19}F relaxation data), as well as for high kinetic inertness (a dissociation half-life of 1285 h is estimated for physiological conditions). The paramagnetic Mn^{2+} leads to a ~150-fold acceleration of the longitudinal ^{19}F relaxation, with moderate line-broadening effect, resulting in T_2/T_1 ratios of 0.8 (9.4 T). Owing to its inner sphere water molecule, **MnL1** is a good ^{1}H relaxation agent as well ($r_1 = 5.36\ mM^{-1}s^{-1}$ at 298 K, 20 MHz). **MnL1** could be readily visualized in ^{19}F MRI by using fast acquisition techniques, both in phantom images and living mice following intramuscular injection, with remarkable signal-to-noise ratios and short acquisition times. While applications in targeted imaging or cell therapy monitoring require further optimisation of the molecular structure, these results argue for the potential of such small, monohydrated and fluorinated Mn^{2+} complexes for combined ^{19}F and ^{1}H MRI detection.

Introduction

Magnetic Resonance Imaging (MRI) based on the detection of water ^{1}H nuclei, highly abundant in tissues, has become the most prominent full-body imaging modality of soft tissues in the clinics. ^{19}F MRI has emerged more recently, providing complementary advantages to ^{1}H detection. The almost complete lack of background signal in biological systems allows for easy localization of ^{19}F containing materials as hotspots in combined $^{19}F/^{1}H$ MRI.[1–2] Further, the broad accessible range (>350 ppm) of ^{19}F chemical shifts offers the possibility of multiplex detection.[3–4] Despite the favorable NMR properties of the ^{19}F nucleus that include good sensitivity and 100 % natural abundance, ^{19}F MRI faces a major challenge related to its in vivo detection sensitivity. This stems from the low local concentration of exogenous ^{19}F MRI probes and from the typically very slow ^{19}F relaxation (in the range of seconds), which requires long acquisition times, often incompatible with in vivo imaging. To improve sensitivity, the most obvious strategy has been the use of nanoparticle probes with high ^{19}F content, based on perfluorocarbons,[5] fluorinated polymers,[6–7] or inorganic fluorides.[8] Some of these offer very good detection capabilities in cell tracking or targeted imaging.[6–7,9–10] In particular, perfluorocarbon nanoemulsions have high fluorine payload and are considered physiologically inert. They naturally tend to accumulate in inflammatory foci,[11] but can be also conjugated with active targeting moieties. For instance, active targeting of the particles combined with frequency differentiation of various fluorinated molecules in the nanoemulsions allowed the simultaneous visualization of several biomarkers in cardiovascular diseases.[4] Multimodal,[12] stimuli-responsive and theranostic[13] applications involving ^{19}F MRI probes are also emerging, but remain often confronted with sensitivity limitations. For further sensitivity enhancement, Ahrens et al. pioneered the use of paramagnetic metal ions incorporated into perfluorocarbon nanoemulsions in the form of tris-β-diketonate complexes. They concluded that among the different metal ions tested, Fe^{3+} provided the most optimal relaxation properties.[14–15]

In contrast to nanoparticles, small molecular probes can present several advantages. These include well-defined, fully characterized and reproducible chemical structures, better water solubility without the need for encapsulation in specific formulations, and more desirable in vivo biodistribu-

[*] Dr. Z. Garda, Dr. F. Szeremeta, O. Quin, R. Clémençon, Dr. S. Même, Prof. C. Pichon, Dr. É. Tóth
Centre de Biophysique Moléculaire, CNRS UPR 4301, Université d'Orléans, rue Charles Sadron, 45071 Orléans, France
E-mail: eva.jakabtoth@cnrs-orleans.fr
zoltan.garda@cnrs-orleans.fr
Dr. Z. Garda, Dr. E. Molnár, B. Váradi, Prof. G. Tircsó
Department of Physical Chemistry, University of Debrecen, Egyetem tér 1, 4010 Debrecen, Hungary
Prof. C. Pichon
Inserm UMS 55 ART ARNm and LI2RSO, University of Orléans, F-45100 Orléans, France
Prof. C. Pichon
Institut Universitaire de France, 1 rue Descartes, F-75035 Paris, France

tion and pharmacokinetic profiles like fast excretion. While such small probes should obviously contain as many as possible magnetically equivalent fluorine atoms in order to have a single and intensive ^{19}F resonance signal, given the lower number of ^{19}F atoms available, it becomes even more critical to accelerate their relaxation than in the case of nanoparticles. For this reason, different paramagnetic metal ions have been applied, both lanthanides and transition metals. Parker et al. demonstrated 10–25-fold sensitivity gains in ^{19}F MRI for Dy, Tb, Ho, Er or Tm complexes when placing the ^{19}F atom at 4.5–7 Å distance from the metal ion.[16–17] Yb and Ce complexes of a macrocyclic chelate with four CF_3 moieties were visualized by ^{19}F MRI in rats.[18] Pierre et al. compared the paramagnetic relaxation rate enhancement and the ^{19}F MRI detection sensitivity for a series of lanthanide and Fe^{2+} complexes of a DOTA-tetraamide ligand bearing four equivalent CF_3 groups.[19] While Ho^{3+} and Fe^{2+} analogues performed best in aqueous solution, in blood, strong T_2 shortening prevented the detection of the Ho^{3+} chelate. Other transition metals, such as Mn^{3+}, Ni^{2+}, Co^{3+} and Cu^{2+} were explored as well; some as redox-sensitive ^{19}F MRI probes involving redox transformation of the metal with MRI detectable consequences on the paramagnetic ^{19}F relaxation effect.[20–25]

Gd^{3+}, providing very strong relaxation effect, has been also combined with ^{19}F-bearing ligands, mostly to derive bioresponsive ^{19}F MRI probes. In this strategy, pioneered by Kikuchi et al. and exemplified by enzymatically activated probes,[26–28] the ^{19}F signal is not observable due to the strong relaxation effect of the proximal Gd^{3+}; it is "turned on" upon enzymatic cleavage of the substrate linker when ^{19}F atoms and Gd^{3+} become distant. The same strategy has been recently extended to perfluorinated nanoparticles by conjugating Gd^{3+} complexes via enzyme-cleavable spacers.[29–30] In an analogous manner, the proximity of other strong relaxation agents, like Mn^{2+},[24] Fe^{3+}[31] or Eu^{2+}[32] were also exploited in redox-responsive probes to mask the ^{19}F signal, which became observable only after redox transformation of the metal ion to a less paramagnetic form which yields slower ^{19}F relaxation.

As opposed to these examples where the strong paramagnetic relaxation effect of Gd^{3+} prevents observation of the ^{19}F signal, it was also possible to detect ^{19}F MRI of fluorinated Gd^{3+} complexes, though this strategy has so far attracted much less attention. By using MRI sequences with ultrashort echo time (UTE) or zero echo time (ZTE) in phantom experiments, Parker, Faber and collaborators demonstrated ^{19}F detection for a fluorinated DO3 A-monoamide Gd^{3+} complex, with a ~27-fold sensitivity gain with respect to diamagnetic analogues,[33] and more recently, Faas et al. visualized the Gd^{3+}-bound state of a fluorinated enzymatic probe.[34] By comparing two complexes, another study concluded that a Gd-^{19}F distance of 9–10 Å was preferable to a shorter, 7.4 Å distance, to produce higher signal to noise ratio in ^{19}F MRI phantoms, at least with a Fast Low Angle Single Shot (FLASH) pulse sequence.[35]

Today all clinical ^1H MRI probes are Gd^{3+} complexes, however, the replacement of Gd^{3+} with more biocompatible metal ions has become an important goal. It is motivated both by toxicity concerns related to Gd^{3+} release[36] and retention[37] in the body and by ecological arguments.[38] Mn^{2+} is the most obvious candidate, and for many years, we have been involved in the development of Mn^{2+}-based contrast agents. Mn^{2+} has a more moderate paramagnetic relaxation effect than Gd^{3+} due to its lower electron spin ($S=5/2$ vs 7/2) and potentially faster electronic relaxation. Here, we have hypothesized that this can be beneficial for the design of ^{19}F MRI probes. In chelates where a high number of magnetically equivalent ^{19}F atoms are placed at an appropriate distance from the metal center, Mn^{2+} would generate maximized relaxation effects which could be efficiently harvested by using ultrafast acquisition sequences. The optimal metal-^{19}F distance should be potentially shorter than in Gd^{3+} complexes. A shorter metal-^{19}F distance can be more easily controlled by rigid ligand structures, in contrast to the previously investigated Gd^{3+} systems characterized by significant internal flexibility, resulting in a large and often uncontrollable range of accessible Gd–F distances. The rigidity of the ligand will be equally important to ensure high kinetic inertness of the Mn^{2+} chelate and to avoid in vivo metal release. Further, the presence of an inner sphere water molecule in the complex can make it applicable in ^1H MRI as well, with advantages of dual ^1H and ^{19}F detection, as it was also highlighted for fluorinated Gd^{3+} complexes.[34–35]

Despite the successful ^{19}F MRI results with perfluorocarbon nanoemulsions, recent findings incriminate perfluoroalkyl substances in general as neuroendocrine disruptors, and their universal persistence in humans and in the ecosystem has been widely evidenced.[39] In this context, it becomes important to scrutinize other strategies to design efficient ^{19}F MRI probes, which can be also relevant to applications other than the in vivo monitoring of labelled cells, where ^{19}F MRI is mostly investigated today. In the objective of exploring the potential of stable, inert, highly fluorinated, and small molecular weight Mn^{2+} chelates as dual ^{19}F and ^1H MRI agents, we have synthesized ligand **L1** and investigated its Mn^{2+} complex (Scheme 1). In **L1**, the cyclohexane backbone and the piperidine rings which involve the metal-coordinating amide groups are both important design elements to provide high rigidity, thus fully controlled Mn–F distance, as well as high kinetic inertness. **MnL1** is expected to contain one inner sphere water

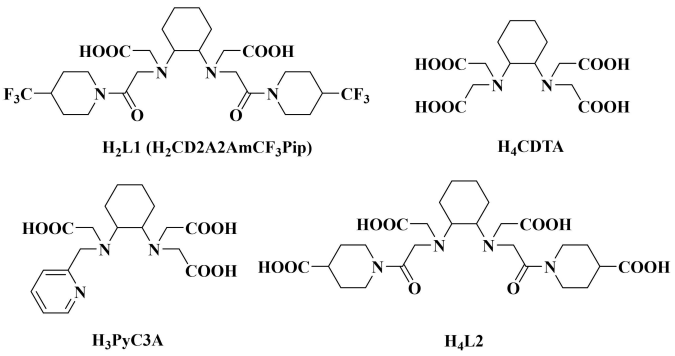

Scheme 1. Ligand structures.

molecule, thus to function as an efficient ^{1}H MRI contrast agent. We show here that this chelate has excellent kinetic inertness, in accordance with our previous data on CDTA-bisamides,[40] and remarkably improved proton relaxation capacity as compared to analogous, small molecular weight Mn^{2+} chelates. The six ^{19}F atoms are incorporated in the molecule at an appropriate distance from the metal in order to take full benefit of the paramagnetic relaxation effect, which results in high signal to noise ratios in ^{19}F MR images recorded with fast acquisition sequences and in very short times. The potential of this small fluorinated Mn^{2+} chelate as a combined ^{1}H and ^{19}F MRI probe is demonstrated in vivo in mice, following intramuscular injection.

Results and Discussion

Synthesis and Characterization of MnL1

Ligands derived from CDTA have been successfully used in recent years for Mn^{2+} complexation, providing good stability, inertness and proton relaxivity. One important example is **MnPyC3A**, currently in clinical phase development as a Mn^{2+} alternative to Gd^{3+}-based ^{1}H MRI contrast agents (Scheme 1).[41] **L1** contains two CF_3 groups introduced in *para* position of piperidine rings which are linked to the ligand skeleton via amide functions. It has been indeed shown that the substitution of carboxylates in CDTA by amide donors increases the kinetic inertness of the Mn^{2+} chelate.[40] **L1** was synthetized in two steps from CDTA through anhydride formation. The reaction of CDTA-dianhydride with 4-(Trifluoromethyl)piperidine resulted in the formation of **L1** which was purified by HPLC (Scheme S1; Figures S1–S6).

Amides are typically resistant to hydrolysis, except for strained structures.[42] In order to verify that the involvement of the amide nitrogen in the piperidine ring has no weakening effect, the stability of the amide bond in **L1** has been verified by ^{19}F NMR measurements. At neutral pH, no significant transformation is observed up to 10 days. Hydrolysis becomes detectable with increasing acidity (Figures S7–S8), however, it remains slow enough and will not perturb the determination of ligand protonation constants and complex stability constants. Conversely, no hydrolysis at all is observable when the ligand is chelated to a metal ion, evidenced by the lack of any change over time in the ^{19}F NMR spectra.

pH-potentiometry was used to determine protonation constants, log K_{Hi} of **L1**, and stability constants, log K_{ML}, of metal complexes formed with Mn^{2+} and some endogenous metal ions (Mg^{2+}, Ca^{2+}, Zn^{2+}; Table S1). The protonation constants evidence lower basicity of the ligand as compared to CDTA, resulting from the strong electron-withdrawing effect of the amide moiety as well as of the CF_3 groups in the side chains (Table 1). The slight increase in log K_{H1} with increasing NaCl ionic strength is related to Na^{+} complex formation as evidenced for the parent CDTA.[43] Stability constants of **ML1** complexes are lower than those of the CDTA analogues (Tables 1 and S1), which also reflects the smaller ligand basicity. In overall, the similar pMn value for **L1** and CDTA is a direct indication of their comparable metal binding capacity. Species distribution curves demonstrate that **MnL1** is the only species in solution near physiological pH (Figure S9).

Table 1: Ligand protonation constants (log K_{Hi}), **MnL** stability constants (log K_{MnL}), and pMn values. $I = 0.15$ M NaCl.

	L1	PyC3A[a]	CDTA[b]
log K_1^H	8.54(2); 8.17(4)[c]	10.16	9.36
log K_2^H	4.95(3); 4.85(5) [c]	6.39	5.95
log K_3^H	2.12(3); 2.09(5) [c	3.13	3.62[d]
log K_{MnL}	12.51(1)	14.14	14.32
log K_{MnL}^H	2.21(2)	2.43	2.90[e]
pMn[f]	**8.17**	**8.17**	**8.68**

[a] ref. [41]; [b] ref. [46]; [c] I = 1.0 M NaCl; [d] log $K_4^H = 2.57$, log $K_5^H = 1.4$; [e] log $K_{MnHL}^H = 1.89$; [f] pMn = –log $[Mn]_{free}$ (pH = 7.4, $c_{Lig} = c_{Mn} = 10\ \mu M$).

The **MnL1** complex was prepared in aqueous solution by mixing equimolar quantities of Mn^{2+} and **L1** and controlling the pH at 7.4 (see Figure S10 for HRMS of **MnL1**). The lipophilicity of the complex, which is increased by the introduction of fluorinated groups, is an important characteristic that guides not only water solubility, but also the biodistribution profile. The shake-flask method with ^{19}F NMR[44] and ICP-OES quantification was used to determine log$P = 0.11$ for **MnL1** (pH 7.3, 298 K; DPBS buffer, Figure S11 and Table S2). Surprisingly, analytical HPLC revealed the existence of three **MnL1** species, characterized by distinct ^{19}F NMR signals (Figures S12–13), which have been tentatively attributed to isomers (diastereomers) that arise from the presence of chiral centers on the cyclohexyldiamine scaffold as well as on the amine nitrogens once coordinated to the metal ion; see Figure S14. Similar situation of isomerization has been previously described for lanthanide(III) complexes of CHXOCTAPA, a 1,2-diaminocyclohexane scaffold functionalized with two acetate and two picolinate pendant arms.[45] In aqueous solution, two major isomers (1 and 3, 44.2 % and 48.7 %, respectively) and one minor isomer (2; 7.1 %) co-exist (pH 7.3, 298 K). They undergo very slow interconversion (~10 % in five days at pH 7.3, 298 K; Figure S15), which allows for their comfortable individual investigation following HPLC separation.

Metal complexes used in medical diagnosis and therapy must have high kinetic inertness, so that they do not dissociate in vivo to release free metal ion. Kinetic inertness of **MnL1** was first assessed in metal exchange reactions induced by 25-fold excess of Zn^{2+} at pH 6, as suggested by Gale et al.[41] Zn^{2+} forms a more stable complex with **L1** than Mn^{2+} (log $K_{ML} = 14.25$ and 12.51, respectively), thus it triggers **MnL1** dissociation, which was followed by measuring ^{1}H T_2 relaxation times. As expected,[40] the substitution of two carboxylates in CDTA by amides provides a substantial, two orders of magnitude gain in kinetic inertness for **MnL1**, with a slightly slower dissociation for Isomer 3 than for Isomer 1 ($t_{1/2} = 47$ h vs. 27 h, Table 2, Figure S16). We gained further insight into the dissociation mechanism by monitoring Cu^{2+} exchange for the **MnL1** isomer mixture

Table 2: Rate and equilibrium constants and half-lives characterizing dissociation of **MnL1** and **MnCDTA** (298 K, 0.15 M NaCl).

	MnL1	MnCDTA[b]
k_1 ($M^{-1}s^{-1}$)	3.8 ± 0.2	400
K_{MnHL}	680 ± 200	-
K_M	11 ± 4	79
$t_{1/2}$ (h)[a] pH 7.4	1285	12
$t_{1/2}$ (h)[c] pH 6.0	51[a] (Isomer mix); 40[d]; 27 (Isomer 1); 47 (Isomer 3)	0.5[a]

[a] from Cu^{2+} exchange; [b] ref. [46]; [c] pH 6.0, 25 equ. Zn^{2+}, 298 K; [d] data were fitted with a single exponential function.

at varying pH (3.50-4.82). The observed rate constants, k_{obs}, increase with H^+ ion concentration, indicating the predominance of acid-assisted dissociation (Figure S17). On the other hand, k_{obs} values slightly diminish with increasing Cu^{2+} concentration, which points to the formation of a slowly dissociating heterodinuclear **MnL1Cu** complex reducing the concentration of the kinetically more active protonated species. Analysis of the experimental k_{obs} data yielded the rate constant for the acid-assisted dissociation, k_1, while the spontaneous dissociation pathway proved to be negligible under these conditions (Table 2, see Supporting Information for details). The dissociation half-life estimated for pH 7.4 is 1285 h, comparable, or even higher than that of highly inert macrocyclic MnPC2A derivatives.[47] In overall, these results confirm good stability and remarkably high inertness of **MnL1**, important to avoid any in vivo toxicity related to free metal ion release. These data have been complemented by cytotoxicity assays on HeLa cells and K-562 lymphoblast cells, which confirmed biocompatibility of **MnL1** with good cell viability up to 2 mM concentration during 24 h (Figures S18–S19). Also, **MnL1** was found to undergo limited cellular internalization in K-562 lymphoblasts (Figure S20).

^1H and ^{19}F Relaxation Properties of MnL1

MnL1 is expected to contain one inner sphere water molecule, thus first we assessed its efficiency as a ^1H MRI relaxation agent. Longitudinal water proton relaxivities, r_1, were measured as a function of the magnetic field (0.01–80 MHz proton Larmor frequencies) at 298 and 310 K for aqueous solutions of both Isomers 1 and 3, as well as for the equilibrium isomer mixture (Figures S21–S23). In addition, variable temperature (275–343 K) ^{17}O transverse relaxation rates and chemical shifts were acquired (Figures 1 and S24). Monohydration of **MnL1** could be confirmed by the maximum values of the ^{17}O relaxation rates (Figure S25).[48] While above 8 MHz the proton relaxivities are identical for the two isomers, at lower fields, they are slightly higher for Isomer 3. This reflects differences in their electron spin relaxation, likely related to different symmetries. The NMRD and the ^{17}O NMR data have been analyzed together according to the common Solomon-Bloembergen-Morgan theory of paramagnetic relaxation (Table S3).[49] The most important parameters calculated from this analysis are the

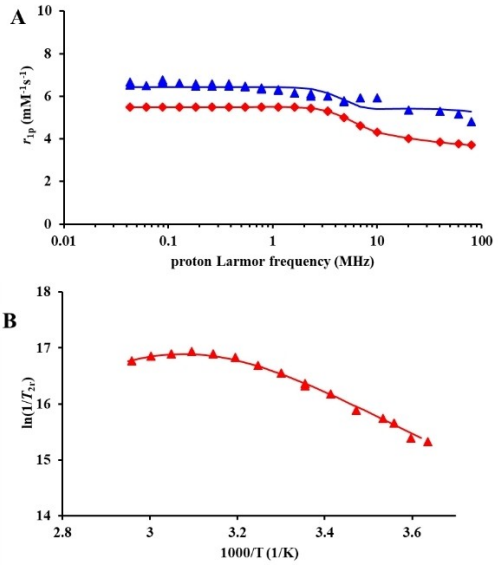

Figure 1. ^1H NMRD profiles at 298 (▲) and 310 K (♦) K (A) and temperature dependent reduced transverse ^{17}O NMR relaxation rates at 9.4 T (B) for **MnL1** (Isomer 1; 2.75 mM). The lines represent the fit of the data.

water exchange rate, k_{ex}^{298}, and the rotational correlation time, τ_{RH}^{298} (Table 3). Water exchange proceeds slightly faster on Isomer 3 than on Isomer 1 ($k_{ex}^{298} = 3.4\times10^7\ s^{-1}$ vs. $1.4\times10^7\ s^{-1}$, respectively), while their rotational dynamics is very similar, in accordance with the identical relaxivity values at high field ($\tau_{RH}^{298} = 136$ ps vs 144 ps for Isomers 3 and 1, respectively). The most relevant information is the remarkable ^1H relaxation efficacy of **MnL1**, ~50–60 % higher than that of **MnCDTA** or **MnPyC3A** (Tables 3). This is the consequence of its increased molecular weight induced by the two piperidine-CF_3 moieties. Similarly high relaxivity was reported for the analogous **MnL2** (Scheme 1, Table 3 and S4).

Next, the paramagnetic effect of Mn^{2+} on ^{19}F relaxation was investigated by measuring ^{19}F relaxation times for free **L1** and for Isomers 1 and 3 of **MnL1**. The ^{19}F NMR spectrum of **L1** contains two signals at −74.69 and −74.58 ppm (Figure S4) which likely originate from different conformations (chair or boat) of the piperidine ring bearing the CF_3 group. These two ^{19}F signals are characterized by

Table 3: ^1H relaxivities (r_{1p}^{298}, 20 MHz) water exchange rates (k_{ex}^{298}) and rotational correlation times (τ_{RH}^{298}) of Mn^{2+} complexes.

	MnL1 Isom1	MnL1 Isom3	MnCDTA [a]	MnL2 [b]	MnPyC3A [c]
r_{1p}^{298} ($mM^{-1}s^{-1}$)	5.36; 3.76[d]	5.26; 3.56[d]	3.6	5.3	2.1[d]
k_{ex}^{298} ($10^6\ s^{-1}$)	14.4	33.6	141	50	53.8
τ_{RH}^{298} (ps)	144	136	74	126	–

[a] ref. [50]; [b] ref. [51]; [c] ref. [41]; [d] 310 K, 1.4 T.

very similar longitudinal (T_1), but considerably different transverse (T_2) relaxation times (9.4 T, 298 K; Table 4). ^{19}F relaxation times of **MnL1** were determined at three field strengths (4.7, 9.4 and 14.1 T). In the **MnL1** ^{19}F spectra, the two signals become also resolved at higher fields (Figure 2). Relaxation times measured on all exploitable ^{19}F signals are listed in Table 4. In overall, Mn^{2+} causes a ~150-fold acceleration of the longitudinal ^{19}F relaxation (9.4 T), with a rather limited variation (<50%) between the different **MnL1** isomers. The paramagnetic effect of Mn^{2+} on T_2 (line-broadening) is relatively moderate, leading to T_2/T_1 ratios in the range of 0.6–0.8 for **MnL1**, which is considered to be adapted for imaging. We note that **MnL1** isomers present slightly different ^{19}F chemical shifts, however, slow isomer interconversion (see above) allows the investigation of individual isomers and avoids problems associated with ^{19}F signal multiplication. Nevertheless, the signal separation at high fields related to the piperidine conformation obviously leads to lower signal intensity.

Table 4: ^{19}F relaxation times of **L1** (pH 7.51) and different isomers of **MnL1** at 4.7, 9.4 and 14.1 T (Isomer 1: 5.5 mM, pH 7.15; Isomer 2: 5.0 mM, pH 7.23; Isomer 3: 5.3 mM, pH 7.37); 10% D_2O; 298 K; $n=3$.

		T_1 (ms)	T_2 (ms)	T_2/T_1
L1	−74.58 ppm	350±7[a]	27±2[a]	0.08[a]
	−74.69 ppm	355±6[a]	89±2[a]	0.25[a]
MnL1	−72.97 ppm	2.03±0.04[b,d]	1.61±0.03[b,d]	0.79[b,d]
Isomer 1		2.18±0.02[a]	1.48±0.02[a]	0.68[a]
		2.81±0.02[c]	1.55±0.03[c]	0.55[c]
	−73.69 ppm	2.83±0.02[a]	1.93±0.02[a]	0.68[a]
		3.87±0.01[c]	2.20±0.02[c]	0.57[c]
MnL1	−73.56 ppm	2.47±0.03[a]	1.93±0.03[a]	0.79[a]
Isomer 2				
MnL1	−73.18 ppm	2.00±0.03[b]	1.60±0.03[b]	0.80[b]
Isomer 3		2.46±0.01[a]	1.78±0.03[a]	0.72[a]
		3.06±0.01[c]	1.92±0.02[c]	0.63[c]

[a] 9.4 T; [b] 4.7 T; [c] 14.1 T, [d] only one peak observed.

The Mn^{2+}-induced paramagnetic ^{19}F relaxation is expected to be dominated by the dipolar contribution, as in the case of Gd^{3+} complexes.[35] At the high magnetic fields applied here, the correlation time that governs this interaction is determined by the rotational motion, and the effect of the electron spin relaxation can be neglected (see Supporting Information). The Mn–F distance, r_{MnF}, can be hence estimated from the field-dependent ^{19}F $1/T_1$ and $1/T_2$ relaxation rates. As in this analysis, r_{MnF} and the rotational correlation time, τ_R, are directly correlated, the latter was fixed to the value obtained above from water proton relaxation data, by using a correction for the internal motion of the water molecule. It has been indeed shown that τ_{RH} determined from ^1H NMRD data is shorter than the rotational correlation time of the entire complex (~70%), due to the rotation of the inner sphere water molecule around the metal–water oxygen axis.[52] In this way, a single $r_{MnF}=8.2\pm0.2$ Å could be calculated for Isomer 3. For Isomer 1, the T_1 and T_2 values determined for the two ^{19}F NMR signals yielded slightly different Mn–F distances, 8.0± 0.2 Å and 8.4±0.2 Å, which might be indicative of two CF_3

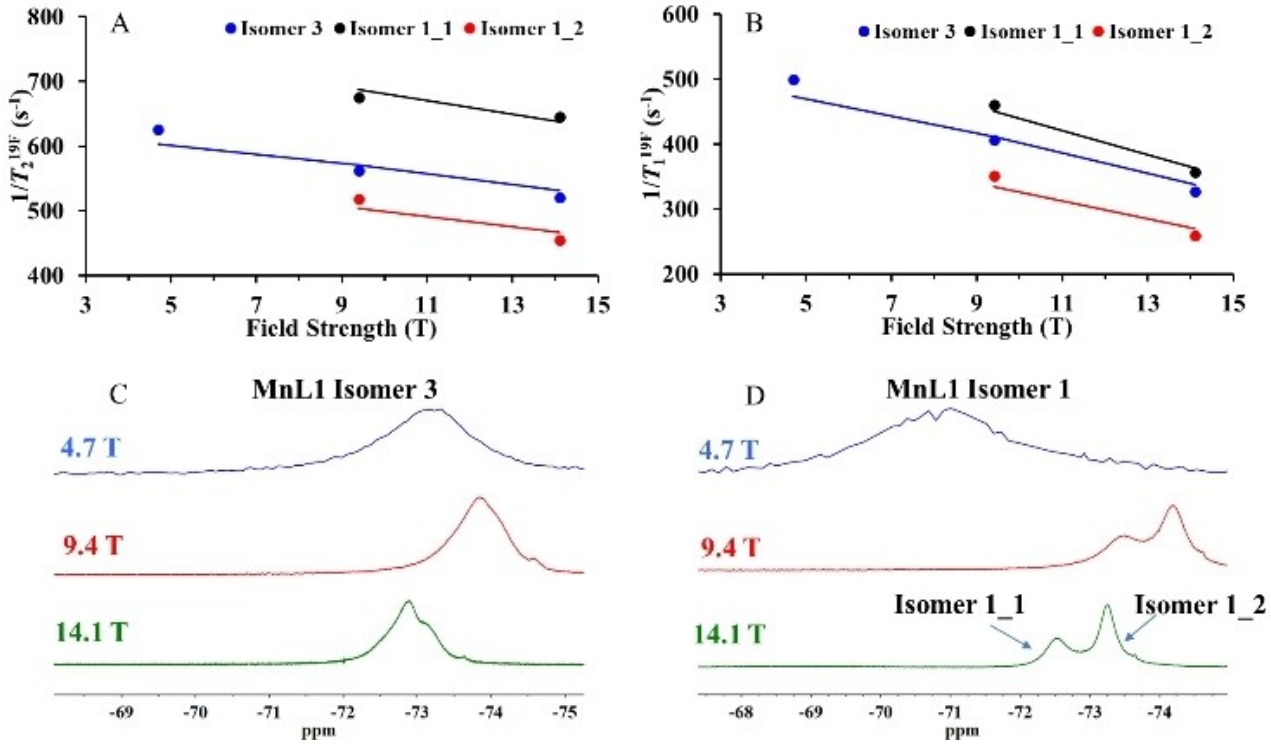

Figure 2. ^{19}F transverse (A) and longitudinal (B) relaxivities as a function of the magnetic field strength (solid lines correspond to the fit of the data). ^{19}F NMR spectra of **MnL1** Isomers 1 (pH 7.15) and 3 (pH 7.37) at different field strengths (C and D) in 10% D_2O. These spectra were not referenced to NaTFA.

groups in different positions depending on the conformation of the piperidine ring (Table S5).

^{1}H and ^{19}F MRI using MnL1

Phantom ^{19}F MR images have been recorded at 7 T for Isomers 1 and 3 of **MnL1** (0–13.7 mM), using a home-made loop gap coil and UTE and FLASH sequences. In all cases, SNR increases linearly with fluorine concentration (Figures 3 and S26–27). The UTE sequence is better adapted to the fast relaxation ($T_1 \sim 2$–4 ms, $T_2 \sim 1.5$–2.2 ms) resulting in excellent signal to noise ratios within short acquisition times (Figure S28); for instance SNR = 12 at 0.41 mM **MnL1** in 1 minute (matrix: 64×64). The better performance of the UTE sequence for **MnL1** is directly demonstrated by comparing the effective $SNR_{eff} = SNR/t^{1/2}$ values (where t is the experimental time in minutes),[53] plotted as a function of the number of ^{19}F atoms per voxel (Figure S29). On the other hand, UTE is not adapted to visualize the ^{19}F signal of the ligand itself, without the paramagnetic metal ion (Figure S27).

In Vivo MR Images

In order to demonstrate the in vivo applicability of small, fluorinated, paramagnetic Mn^{2+} complexes for ^{19}F MRI, allowing ^{1}H detection as well, **MnL1** (Isomer 1) was injected intramuscularly into the right hind leg of 5C57BL/6 mice (40 µL of **MnL**1 at 2.1 mM or 8.2 mM concentrations). Since **MnL1** has no specific targeting or cell labelling capability, the aim of this proof-of-concept experiment was to test if ^{19}F MRI detection is feasible within reasonable acquisition times, upon the injection of ^{19}F quantities which are comparable to those typically used for instance in in vivo ^{19}F MRI detection of cells pre-labelled with ^{19}F probes, typically perfluorinated nanoemulsions.

When injecting 40 µL of 2.1 mM solution of **MnL1** into the muscle, ^{19}F MR images with an excellent signal to noise ratio and good matrix size (128×128) could be recorded in 8 mins (Figure 4). The ^{19}F amount administered in our experiment (~3×10^{17} ^{19}F atoms) is lower than that used for instance for the successful in vivo visualization of Fe^{2+} containing fluorinated nanoemulsions injected in the form of labelled cells (~10^{19} ^{19}F injected)[14] or ^{19}F labelled gold nanoparticles (~10^{18} ^{19}F injected).[7] Injection of more concentrated solutions (8.2 mM) provided considerably better signal intensity (Figures S30 and S31). Importantly, the localization of the imaging probe is easily and unambiguously achieved by recording a ^{1}H MR image. Indeed, **MnL1** also acts as an efficient water proton relaxation agent, yielding significant signal enhancement in T_1 weighted images. Although not investigated, the probe is expected to undergo mixed renal and hepatobiliary excretion, as reported for a small Mn^{2+} complex bearing two CF_3 moieties upon intravenous injection.[54]

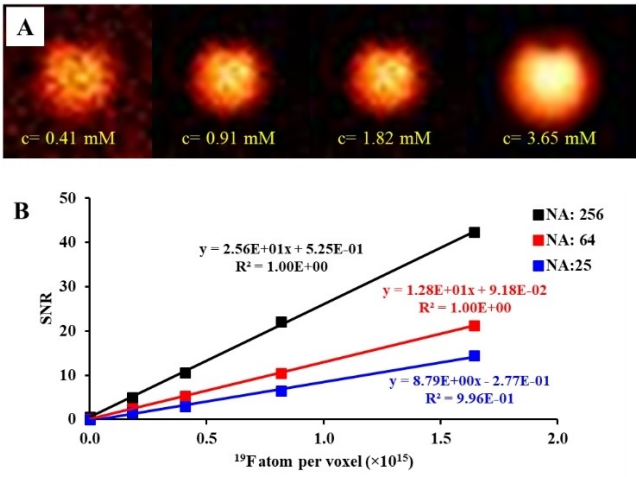

Figure 3. **A**: ^{19}F phantom MR images of **MnL1** (Isomer 1) acquired at different concentrations with UTE sequence at 7 T (matrix size 128×128, NA: 256). **B**: Calculated SNR values (see Supporting Information for SNR calculation) at different numbers of accumulation (NA) plotted as a function of fluorine concentration (number of ^{19}F atoms per voxel). Reconstruction/acquisition matrix 128×128, TR 6.2 ms; TE 0.362 ms; BW 20 kHz; field of view 3.2×3.2 cm; slice thickness 2 mm; NA 256 (10 min 41 sec), 64 (2 min 40 sec) and 25 (1 min 2 sec); FA: 90°.

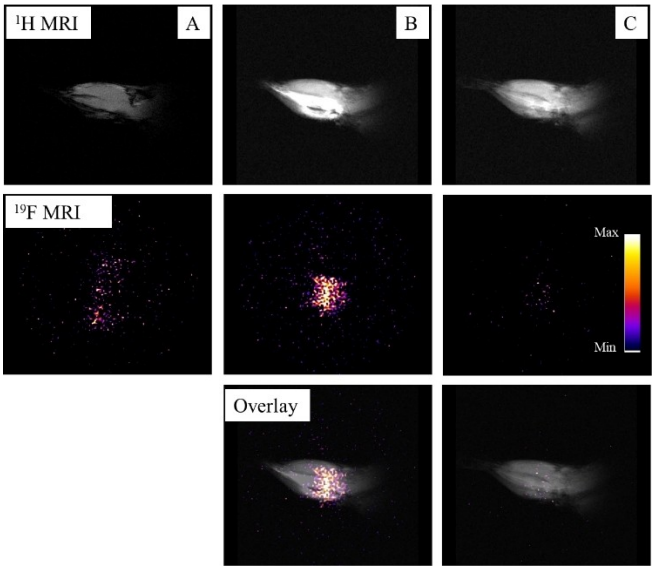

Figure 4. In vivo coronal MR images (^{1}H FLASH, ^{19}F UTE) of a mouse hind leg before and after intramuscular injection of **MnL1** (Isomer 1; 40 µl, 2.1 mM). **A**: Before injection; **B**: after injection (10 min p.i. for ^{1}H and 26 min p.i. for ^{19}F); **C**: 2 hours post injection. ^{1}H and ^{19}F MRI overlay is shown with 50% transparency. ^{1}H FLASH with T1 contrast: flip angle 70°; TR 131.1 ms; TE 5.4 ms; field of view 3.2 cm×3.2 cm; slice thickness 1 mm (on the images 5 slices were summed, covering same volume as UTE), NA 4 (2 min 14 sec); reconstruction/acquisition matrix 256×256. ^{19}F UTE: flip angle 90°; TR 6.5 ms; TE 0.458 ms; field of view 3.2 cm×3.2 cm; slice thickness 5 mm; NA 200 (8 min 45 sec); reconstruction/acquisition matrix 128×128. The fluorine background (before injection) was subtracted from post injection images.

Conclusion

In the objective of proposing new alternatives in ^{19}F MRI, we have designed a small Mn^{2+} chelate, **MnL1**, that contains six fluorine atoms endowed with rapid relaxation. The cyclohexane backbone and the piperidine rings, which involve the metal-coordinating amide groups, provide high rigidity to the complex, and this is important both to achieve a remarkably high inertness and to maintain an optimal distance between Mn^{2+} and the ^{19}F atoms. The proximity of the paramagnetic metal ion causes a ~150-fold acceleration of the longitudinal ^{19}F relaxation, while the line-broadening (T_2 decrease) remains relatively moderate, resulting in T_2/T_1 ratios in the range of 0.6–0.8. Thanks to its inner sphere water molecule, **MnL1** is also an efficient ^{1}H relaxation agent, with ~50 % more elevated proton relaxivities as compared to typical, monohydrated small molecular weight Mn^{2+} complexes. Phantom ^{19}F MR images evidence, in particular when using fast acquisition sequences (UTE), excellent signal-to-noise ratios which linearly increase with **MnL1** concentration. Most importantly, we demonstrate that upon intramuscular injection of **MnL1** into the mouse leg, the ^{19}F content is readily visualized in short acquisition times, and that the ability of the complex to act as a ^{1}H contrast agent makes probe localization easy. While our system has to be further adapted to biomedically relevant ^{19}F imaging applications (specific targeting, cell labelling), these results demonstrate the potential of small molecular weight, paramagnetic Mn^{2+} complexes in ^{19}F MRI, which can be easily combined with ^{1}H MRI contrast enhancement as well.

Supporting Information

The authors have cited additional references within the Supporting Information.[40–41,44,49–51,55–66]

Acknowledgements

We acknowledge financial support of the CNRS, the Hungarian National Research, Development and Innovation Office (NKFIH PD-138064 (ZG) and K-134694 (GyT) projects), and the University of Debrecen Publication Fund. ZG received funding from the European Union's Horizon 2021 research and innovation programme under the Marie Skłodowska-Curie grant agreement No. 101065389. The authors thank Csilla Noémi Tóth and Agnès Pallier for ICP data, Zsolt Szilágyi (University of Debrecen) for contributing to the physical chemical investigation, Vincent Sarou-Kanian (CEMHTI, CNRS Orléans) for ^{19}F relaxation measurements at 200 MHz, and Sara Lacerda for useful discussions.

Conflict of Interest

The authors declare no conflict of interest.

Data Availability Statement

The data that support the findings of this study are available in the supplementary material of this article.

Keywords: ^{19}F MRI · manganese · contrast agent · paramagnetic · ^{1}H MRI

[1] J. W. M. Bulte, *Nat. Biotechnol.* **2005**, *23*, 945–946.
[2] P. Bouvain, S. Temme, U. Flögel, *Wiley Interdiscip. Rev. Nanomed. Nanobiotechnol.* **2020**, *12*.
[3] D. X. Chen, J. N. Guo, A. Li, C. J. Sun, H. B. Lin, H. Y. Lin, C. Y. Yang, W. Wang, J. H. Gao, *Sci. Adv.* **2023**, *9*.
[4] U. Flögel, S. Temme, C. Jacoby, T. Oerther, P. Keul, V. Flocke, X. Wang, F. Bönner, F. Nienhaus, K. Peter, J. Schrader, M. Grandoch, M. Kelm, B. Levkau, *Nat. Commun.* **2021**, *12*, 5847.
[5] J. M. Joseph, M. R. Gigliobianco, B. M. Firouzabadi, R. Censi, P. Di Martino, *Pharmaceutica* **2022**, *14*.
[6] C. Zhang, S. S. Moonshi, W. Wang, H. T. Ta, Y. Han, F. Y. Han, H. Peng, P. Král, B. E. Rolfe, J. J. Gooding, K. Gaus, A. K. Whittaker, *ACS Nano* **2018**, *12*, 9162–9176.
[7] J. M. Arango, D. Padro, J. Blanco, S. Lopez-Fernandez, P. Castellnou, P. Villa-Valverde, J. Ruiz-Cabello, A. Martin, M. Carril, *ACS Appl. Mater. Interfaces* **2021**, *13*, 12941–12949.
[8] A. Galisova, A. Bar-Shir, *Chem. Commun.* **2023**, *59*, 5502–5513.
[9] D. V. Hingorani, F. Chapelin, E. Stares, S. R. Adams, H. Okada, E. T. Ahrens, *Magn. Reson. Med.* **2020**, *83*, 974–987.
[10] J. M. Janjic, M. Srinivas, D. K. K. Kadayakkara, E. T. Ahrens, *J. Am. Chem. Soc.* **2008**, *130*, 2832–2841.
[11] U. Flögel, Z. Ding, H. Hardung, S. Jander, G. Reichmann, C. Jacoby, R. Schubert, J. Schrader, *Circulation* **2008**, *118*, 140–148.
[12] J. Dawid, T. Krawczyk, *Chem. Eur. J.* **2022**, *28*.
[13] M. H. Cho, S. H. Shin, S. H. Park, D. K. Kadayakkara, D. Kim, Y. Choi, *Bioconjugate Chem.* **2019**, *30*, 2502–2518.
[14] A. A. Kislukhin, H. Xu, S. R. Adams, K. H. Narsinh, R. Y. Tsien, E. T. Ahrens, *Nat. Mater.* **2016**, *15*, 662–668.
[15] C. Wang, S. R. Adams, H. Xu, W. Zhu, E. T. Ahrens, *ACS Appl. Bio Mat.* **2019**, *2*, 3836–3842.
[16] K. H. Chalmers, E. De Luca, N. H. M. Hogg, A. M. Kenwright, I. Kuprov, D. Parker, M. Botta, J. I. Wilson, A. M. Blamire, *Chem. Eur. J.* **2010**, *16*, 134–148.
[17] K. H. Chalmers, A. M. Kenwright, D. Parker, A. M. Blamire, *Magn. Res. Med.* **2011**, *66*, 931–936.
[18] V. Herynek, M. Martinisková, Y. Bobrova, A. Gálisová, J. Kotek, P. Hermann, F. Koucký, D. Jirák, M. Hájek, *Magn. Reson. Mater. Phys. Biol. Med.* **2019**, *32*, 115–122.
[19] K. Srivastava, E. A. Weitz, K. L. Peterson, M. Marjańska, V. C. Pierre, *Inorg. Chem.* **2017**, *56*, 1546–1557.
[20] S. M. A. Pinto, A. R. R. Ferreira, D. S. S. Teixeira, S. C. C. Nunes, A. L. M. Batista de Carvalho, J. M. S. Almeida, Z. Garda, A. Pallier, A. A. C. C. Pais, C. M. A. Brett, É. Tóth, M. P. M. Marques, M. M. Pereira, C. F. G. C. Geraldes, *Chem. Eur. J.* **2023**, *29*, e202301442.
[21] F. Koucký, J. Kotek, I. Císařová, J. Havlíčková, V. Kubíček, P. Hermann, *Dalton Trans.* **2023**, *52*, 12208–12223.
[22] J. Blahut, K. Bernášek, A. Gálisová, V. Herynek, I. Císařová, J. Kotek, J. Lang, S. Matějková, P. Hermann, *Inorg. Chem.* **2017**, *56*, 13337–13348.
[23] D. Xie, M. Yu, R. T. Kadakia, E. L. Que, *Acc. Chem. Res.* **2020**, *53*, 2–10.
[24] H. Chen, X. Tang, X. Gong, D. Chen, A. Li, C. Sun, H. Lin, J. Gao, *Chem. Commun.* **2020**, *56*, 4106–4109.

[25] A. Li, X. Luo, D. Chen, L. Li, H. Lin, J. Gao, *Anal. Chem.* **2023**, *95*, 70–82.
[26] J. Salaam, M. Minoshima, K. Kikuchi, *Anal. & Sens.* **2023**, *3*, e202200081.
[27] S. Mizukami, R. Takikawa, F. Sugihara, Y. Hori, H. Tochio, M. Wälchli, M. Shirakawa, K. Kikuchi, *J. Am. Chem. Soc.* **2008**, *130*, 794-+.
[28] S. Mizukami, H. Matsushita, R. Takikawa, F. Sugihara, M. Shirakawa, K. Kikuchi, *Chem. Sci.* **2011**, *2*, 1151–1155.
[29] K. Akazawa, F. Sugihara, T. Nakamura, S. Mizukami, K. Kikuchi, *Bioconjugate Chem.* **2018**, *29*, 1720–1728.
[30] K. Akazawa, F. Sugihara, M. Minoshima, S. Mizukami, K. Kikuchi, *Chem. Commun.* **2018**, *54*, 11785–11788.
[31] R. T. Kadakia, R. T. Ryan, D. J. Cooke, E. L. Que, *Chem. Sci.* **2023**, *14*, 5099–5105.
[32] S. Subasinghe, C. J. Ortiz, J. Romero, C. L. Ward, A. G. Sertage, L. Kurenbekova, J. T. Yustein, R. G. Pautler, M. J. Allen, *PNAS* **2023**, *120*.
[33] F. Schmid, C. Höltke, D. Parker, C. Faber, *Magn. Res. Med.* **2013**, *69*, 1056–1062.
[34] H. M. Faas, J. L. Krupa, A. J. Taylor, F. Zamberlan, C. J. Philp, H. E. L. Williams, S. R. Johnson, G. E. Pavlovskaya, N. R. Thomas, T. Meersmann, *Contr. Med. Mol. Imag.* **2019**.
[35] R. Pujales-Paradela, T. Savić, D. Esteban-Gómez, G. Angelovski, F. Carniato, M. Botta, C. Platas-Iglesias, *Chem. Eur. J.* **2019**, *25*, 4782–4792.
[36] T. Grobner, *Nephrol. Dial. Transplant.* **2006**, *21*, 1104–1108.
[37] E. Di Gregorio, G. Ferrauto, C. Furlan, S. Lanzardo, R. Nuzzi, E. Gianolio, S. Aime, *Invest. Radiol.* **2018**, *53*, 167–172.
[38] H. M. Dekker, G. J. Stroomberg, A. J. Van der Molen, M. Prokop, *Insights into Imaging* **2024**, *15*, 62.
[39] A. Cardenas, R. Hauser, D. R. Gold, K. P. Kleinman, M. F. Hivert, A. F. Fleisch, P. D. Lin, A. M. Calafat, T. F. Webster, E. S. Horton, E. Oken, *JAMA Netw Open* **2018**, e181493–e181493.
[40] Z. Baranyai, Z. Garda, F. K. Kálmán, L. Krusper, G. Tircsó, S. Ghiani, A. Maiocchi, Vol. *WO2016135234*, University of Debrecen [HU]; Bracco Imaging SPA [IT], **2016**.
[41] E. M. Gale, I. P. Atanasova, F. Blasi, I. Ay, P. Caravan, *J. Am. Chem. Soc.* **2015**, *137*, 15548–15557.
[42] K. Tani, B. M. Stoltz, *Nature* **2006**, *441*, 731–734.
[43] J. D. Carr, D. G. Swartzfager, *Anal. Chem.* **1971**, *43*, 1520–1522.
[44] B. Linclau, Z. Wang, G. Compain, V. Paumelle, C. Q. Fontenelle, N. Wells, A. Weymouth-Wilson, *Angew. Chem. Int. Ed.* **2016**, *55*, 674–678.
[45] F. Lucio-Martínez, Z. Garda, B. Váradi, F. K. Kálmán, D. Esteban-Gómez, É. Tóth, G. Tircsó, C. Platas-Iglesias, *Inorg. Chem.* **2022**, *61*, 5157–5171.
[46] F. K. Kálmán, G. Tircsó, *Inorg. Chem.* **2012**, *51*, 10065–10067.
[47] F. K. Kálmán, V. Nagy, B. Váradi, Z. Garda, E. Molnár, G. Trencsényi, J. Kiss, S. Même, W. Même, É. Tóth, G. Tircsó, *J. Med. Chem.* **2020**, *63*, 6057–6065.
[48] E. M. Gale, J. Zhu, P. Caravan, *J. Am. Chem. Soc.* **2013**, *135*, 18600–18608.
[49] E. Toth, L. Helm, A. Merbach, in *The Chemistry of Contrast Agents in Medical Magnetic resonance Imaging*, Second Edition ed. (Eds.: A. Merbach, L. Helm, E. Toth), John Wiley & Sons, Chichester, **2013**, pp. 25–81.
[50] E. Molnár, B. Váradi, Z. Garda, R. Botár, F. K. Kálmán, É. Tóth, C. Platas-Iglesias, I. Tóth, E. Brücher, G. Tircsó, *Inorg. Chim. Acta* **2018**, *472*, 254–263.
[51] D. Lalli, G. Ferrauto, E. Terreno, F. Carniato, M. Botta, *J. Mater. Chem. B* **2021**, *9*, 8994–9004.
[52] F. A. Dunand, A. Borel, A. E. Merbach, *J. Am. Chem. Soc.* **2002**, *124*, 710–716.
[53] W. Sonia, T. R. Jens, K. Andre, S. Ludger, D. Paula Ramos, M. M. Jason, P. Christian, S. P. João, P. Andreas, W. Helmar, *Magn. Reson. Mater. Phys. Biol. Med.* **2018**, *32*, 37–49.
[54] S. W. McRae, M. Cleary, D. DeRoche, F. M. Martinez, Y. Xia, P. Caravan, E. M. Gale, J. A. Ronald, T. J. Scholl, *J. Med. Chem.* **2023**, *66*, 6567–6576.
[55] D. M. Corsi, C. Platas-Iglesias, H. v. Bekkum, J. A. Peters, *Magn. Reson. Chem.* **2001**, *39*, 723–726.
[56] D. F. Evans, *J. Am. Chem. Soc.* **1959**, 2003–2005.
[57] D. F. Evans, G. V. Fazakerley, R. F. Phillips, *J. Chem. Soc. A: Inorg. Phys. Theor.* **1971**, 1931–1934.
[58] H. E. Gottlieb, V. Kotlyar, A. Nudelman, *J. Org. Chem.* **1997**, *62*, 7512–7515.
[59] A. D. Hugi, L. Helm, A. E. Merbach, *Helv. Chim. Acta* **1985**, *68*, 508–521.
[60] H. M. Irving, M. G. Miles, L. D. Pettit, *Anal. Chim. Acta* **1967**, *38*, 475–488.
[61] S. Meiboom, D. Gill, *Rev. Sci. Instrum.* **1958**, *29*, 688–691.
[62] K. Naka, Y. Tanaka, K. Yamasaki, A. Ohki, Y. Chujo, S. Maeda, *Bull. Chem. Soc. Jpn.* **2002**, *74*, 571–577.
[63] J. A. Peters, J. Huskens, D. J. Raber, *Progr. NMR Spectr.* **1996**, *28*, 283–350.
[64] D. S. Raiford, C. L. Fisk, E. D. Becker, *Anal. Chem.* **1979**, *51*, 2050–2051.
[65] C. Vanasschen, E. Molnár, G. Tircsó, F. K. Kálmán, É. Tóth, M. Brandt, H. H. Coenen, B. Neumaier, *Inorg. Chem.* **2017**, *56*, 7746–7760.
[66] L. Zekany, I. Nagypal, in *Computational Methods for the Determination of Formation Constants* (Ed.: D. J. Leggett), Springer US, Boston, MA, **1985**, pp. 291–353.

Manuscript received: June 11, 2024
Accepted manuscript online: July 31, 2024
Version of record online: September 10, 2024